FATIGUE AND FRACTURE ANALYSIS OF A SEVEN-WIRE STAINLESS STEEL STRAND UNDER AXIAL AND BENDING LOADS

D. Erena[1]*, J. Vazquéz[1], C. Navarro[1], J. Domínguez[1]

[1] University of Seville, Mechanical Engineering Department, Camino de los descubrimientos s/n, 41092, Seville, Spain

* Corresponding author, E-mail address: deg@us.es

ABSTRACT

Fatigue failure of cables and strands is a common and complex problem. Failure is typically caused by different combinations of time-variable bending and axial forces. In addition to these loads, contact stresses between wires may play an important role in the fatigue failure of cables. The present work aims to provide deep insight into the fatigue failure of a 7-wire stainless steel strand subjected to a combination of variable axial and bending loads. To avoid side effects in the analysis, fatigue failure of the strand close to the clamps is prevented. Several tests were performed with a new device specifically designed to avoid failure near the clamps. Thus, failure is always produced at the middle length of the specimen. Test simulations were performed by employing the finite element method. The numerical results were validated via comparisons with experimental data. Finally, life prediction curves were obtained.

KEYWORDS: Strand, Life prediction, Numerical model

NOMENCLATURE: C_L = Load factor; d_{min} = Minimum bending displacement; d_{max} = Maximum bending displacement; E = Young modulus ; K_s = Spring stiffness; L_b = Beam element length; L_e =Effective length; L_s = Solid element length; P = Axial load; P_a = Axial load amplitude; P_m = Mean axial load; P_{max} = Maximum axial load; P_{min} = Minimum axial load, P_{mt} = Theoretical mean axial load; Ps = Spring load; P_{sw}= Simplified model spring load; $Q(t)$ = Bending load; s = Longitudinal path coordinate; σ_a = Stress amplitude; $\sigma_{a,eq}$ = Equivalent amplitude stress; σ_m = Mean stress; σ_{uts}= Ultimate strength; σ_{max}= Maximum elastic-plastic stress; σ_{min} = Minimum elastic plastic stress; σ_{max}^e = Maximum elastic axial load; σ_{min}^e = Minimum elastic axial load; Δd = Bending displacement range; $\Delta\sigma_e$ = Elastic stress range; μ = Friction coefficient;

1. INTRODUCTION

The failure of structural and electrical power line cables usually occurs due to fatigue phenomena [1]. Cables are subjected to a combination of axial and bending loads. Bending loads are mainly produced by wind or are induced by mechanical systems [2-4]. The relative movements between wires and strands produce different fretting phenomena such as fretting fatigue [5–8] and fretting wear [9], which can reduce the fatigue strength of cables. Many theoretical and experimental studies have focused on the fatigue life in steel cables, and particular attention has been paid to fretting phenomena. Hobbs et al. [10] developed a semi-analytical procedure to determine stresses in cable wires under axial loads taking into account tangential and normal contact stresses. Subsequently, a fatigue procedure was proposed that included contact stresses from sliding with friction [11], extending later the procedure to bending loads [12].

Zhou et al. [1] performed several tests with electrical power line cables which proved that fretting was a determining factor in the fatigue design of cables. They noticed a relevant effect on fatigue life produced by the type of clamps used to hold the cables.

Recently, Araujo et al. [5], [13] developed a bending fatigue test for aluminium cables to determine the relation between mean stress and fatigue strength. They obtained several S-N curves for different mean stress, but did not discuss the influence of the contact stresses on fatigue strength in detail.

In investigation on the mechanical behaviour of cables, numerous analytical and numerical techniques were employed [14-16]. Analytical techniques are based on elasticity theory, and thus assume some behaviour simplifications. These models are useful for estimating the global behaviour of the cable. However, these models do not take into account non-linear effects or mechanical contacts. Accordingly, it is difficult to accurately analyse the fatigue behaviour of cables from an analytical perspective because many simplifications must be assumed.

Currently, thanks to the increase in computing power, it is less time consuming to attempt to numerically reproduce the real behaviour of cables including all parameters that influence the mechanical behaviour of these elements. However, this is a challenging task because of the complex geometries of cables and the difficulties associated with obtaining a high quality mesh, which is necessary to accurately reproduce the stress/strain fields that are produced in the cable.

Although several studies have been carried out using finite element formulation [17–21], only a few have developed accurate finite element models (FEM) including friction, plasticity and a good mesh refinement around contact zones [22-23]. Nevertheless, although these models reproduce the global response and contacts stresses between cables with high accuracy and low computational cost, the use of these models is limited since it requires a complex mathematical implementation.

Almost all the aforementioned studies investigated the fatigue and fretting behaviour of cables and strands which consist of several wire layer or strands, therefore two types of contact must be considered (*Figure. 1*): a) continuous helical contact that is produced between the wires of the first layer of a strand (see *Figure 1c*); and b) trellis contact that arises between the strands of a cable (see *Figure 1d*) and between the external wire layers of each strand if there is more than one. Therefore, in addition to the complexity associated with the geometry, two different types of contact could appear. *Figure 1a* shows an image took with a scanning electron microscope (SEM) of one of the contact pairs shown in *Figure 1c*, in which a continuous helical contact is observed. Figure. 1b shows an example of a trellis contact mark, with an elliptical shape of one of the trellis contact marked in *Figure 1d*.
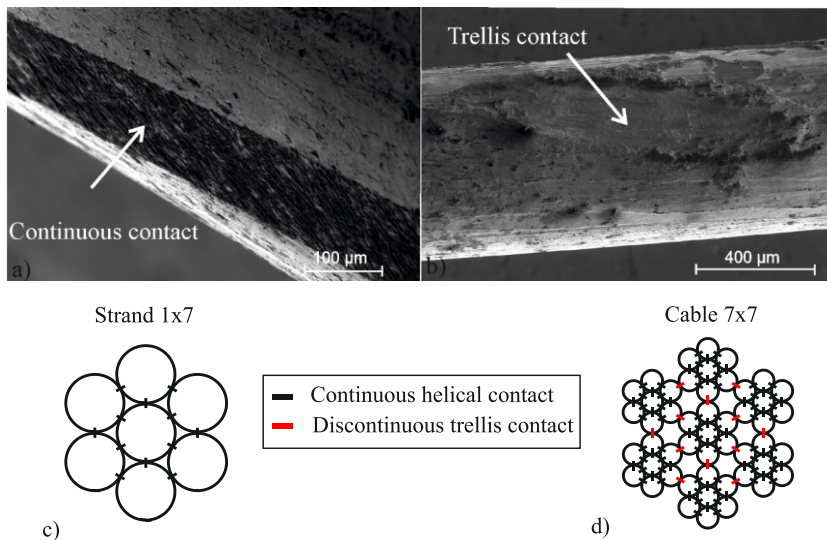

Figure 1. a) SEM image of a continuous helical contact, b) SEM image of a discontinuous trellis contact, c) Strand 1x7 contact pairs type, d) cable 7x7 contact pairs type

Focusing on fretting, the mechanical behaviour of each contact type is different. Continuous helical contact is produced along the total length of the strand. Trellis contact forms a discontinuous pattern of elliptic contact zones along the cable. For both contact types, the contact area and stresses depend on the normal pressure between the wires and the lay angle.

The objective of the present work is to analyse the fatigue behaviour of a 7-wire stainless steel strand (*Figure 1c*) subjected to axial and bending loads, focusing on the interactions between wires. The efforts are focused on the development of a faithful numerical model of the strand to obtain the stress/strain fields. Numerical results combined with experimental fatigue test are used to attempt to predict the fatigue life of strands while accounting for both global and contact stresses. Due to the strand type considered in the present work, the only contact analysed between wires is the continuous one produced along the helix contact lines between the inner wire and the outer wires.

A similar study was performed by Winkler et al. in which a 7-wire steel strand was tested under axial and bending loads [8]. In that work, the axial load increased with the applied bending force, that is, the longitudinal displacement at both ends of the strand was restricted. However, failure of the cable was observed inside the clamp system that was used to hold the strand by means of external pressure. The failure was mainly caused by the fretting fatigue phenomena, which shows that the type of assembly and the boundary conditions of the clamps play a dominant role in cables fatigue life.

2. EXPERIMENTAL METHODOLOGY.

Fatigue tests are performed with a device designed specifically for testing cables and strands [24]. *Figure 2* shows a scheme of the test device used. A variable bending moment is applied at the middle length of the strand by means of the force $Q(t)$ through a bearing sheave of radius 25 mm, while an almost constant axial load P is applied at one end of the specimen. Large displacements are produced by the bending load, making difficult achieve a constant axial load. Cylinder 1 in *Figure 2* is force controlled by imposing a constant axial load P. Nevertheless, due to the synchronization of both hydraulic cylinders and the inherent stiffness of the assembly the system control cannot maintain a completely constant axial load. Therefore, a small axial load amplitude P_a appears and must be taken into account

in conjunction with a mean axial load P_m. The degrees of freedom allowed in the test device are as follows: all rotations on both sides of the specimen and the longitudinal displacement at the right side of the strand, which is necessary to apply the axial load by means of hydraulic cylinder 1. The effective length L_e is measured between both support points (see *Figure 2*). These support points are included to avoid the introduction of transverse inertial forces that appears with the movement of the load cell, which is directly attached to the strand. Additionally, the diameters of the sheaves used as support points are two times the diameter of the punch sheave to avoid failure at these points.

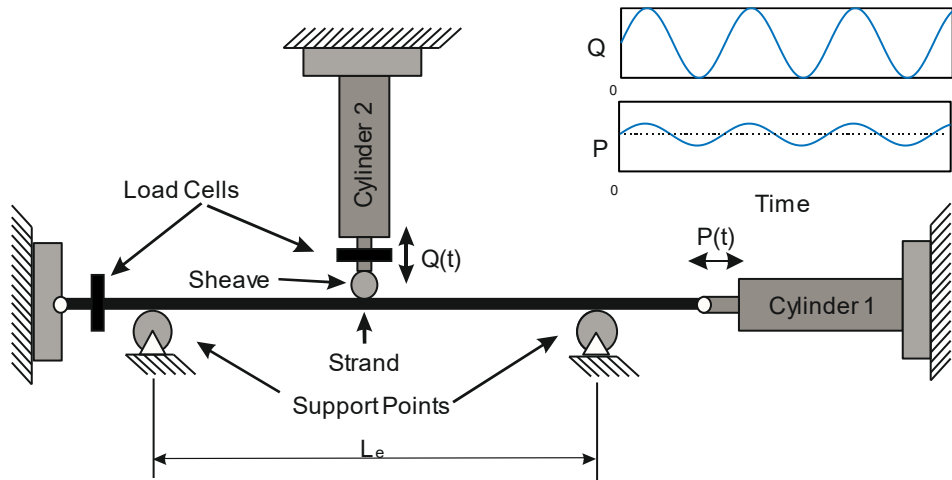*Figure 2. Scheme of the testing machine.*

The bending moment and axial load produce global and contact stresses that lead to failure of the strand in the middle of the effective length. The test stops with the failure of one of the seven wires. The strand used is a 7-wire stainless steel strand (AISI 316). The chemical composition of the stainless steel according to UNE-EN 10264-4:2012 is shown in *Table 1*.

Table 1. AISI 316 chemical composition.

Element	C	Si (max.)	Mn (max.)	P (max.)	S (max.)	Cr	Mo	Ni	N
Weight (%)	≤0.07	1.00	2.00	0.045	0.015	17-19	2-2.5	10-13	≤0.11

The external diameter of the strand is approximately of 4.8 mm. *Figure 3* shows a scheme of the strand cross-section, its relative position to the punch and the index number assigned to each wire. The diameter of Wire 1 in *Figure 3* is 1.7 mm and the diameter of the remaining wires are 1.62 mm. The lay angle α forms 14º degrees with the axis of the strand. The value of the maximum tensile stress (σ_{uts}) is approximately 1600 MPa. In all tests, the effective length of the specimen L_e is 980 mm.
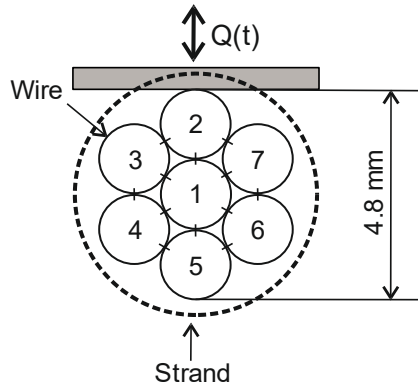
Figure 3. Strand cross-secction geometry.

To investigate the influence of mean axial stress on fatigue life, the test mean axial load, P_m, is varied from 2 kN up to 6 kN. The cyclic load Q, which produces the bending moment, is applied by a predefined displacement range Δd. The maximum displacement dmax ranges from 20 to 50 millimetres depending on the test, being the minimum displacement dmin zero. The load Q is known during the test thanks to the cylinder 2 load cell (see *Figure 2*). Test results are shown in *Table 2*.

After the tests, fracture surfaces are visually inspected, and it is noted that the fracture surfaces in all cases are nearly transversal to the longitudinal axis. In addition, the wire fractures are always located at the middle length of the specimen. Fretting wear and a significant amount of fretting debris is observed along the helical contact lines between wires as shown in Figure 1a. To obtain more information, fracture surfaces are studied using a scanning electron microscope (SEM) for thorough analysis specifically regarding crack initiation points and its corresponding propagation. In most cases, the outer wire in the lowest position (wire 5 in *Figure 3*) is the first to break (75% cases); in other cases, Wire 5 and Wire 1 break at the same time. *Figure 4* shows SEM images in which crack initiation points and crack growth directions can be observed.
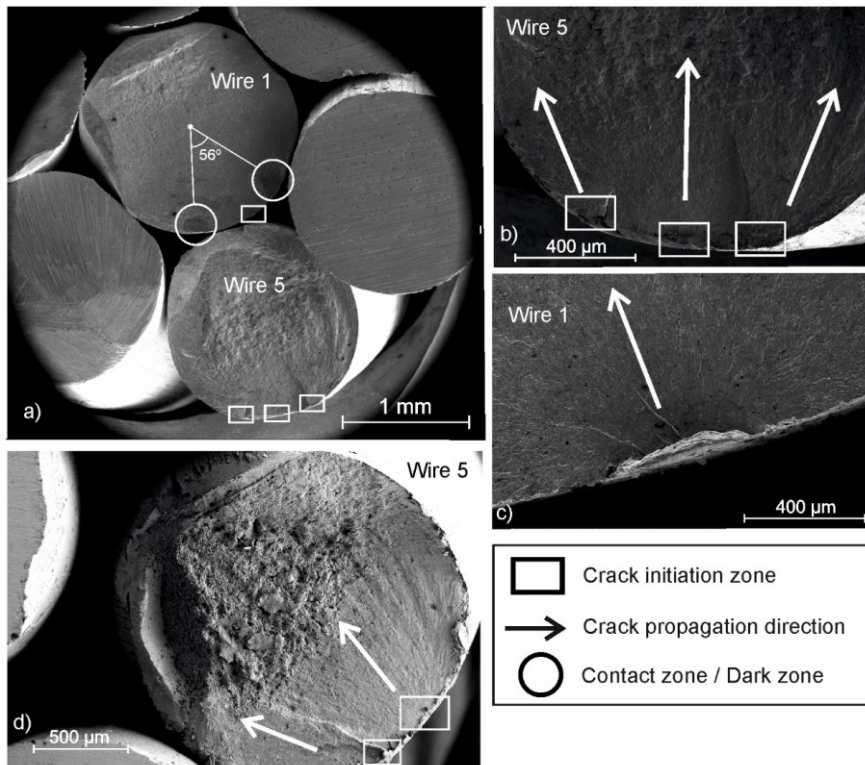

Figure 4. SEM images. a) Test 1 strand, b) Test 1 Wire 5 detail, c) Test 1 Wire 1 crack initiation detail, d) Test 34 Wire 5 detail. (see Table 1).

Figure 4a to *Figure 4c* correspond to test number 1 (see *Table 2* for test data). Up to three well-differentiated initial cracks are observed in Wire 5 (see *Figure 4b*), which initiate at the free surface, where no contact exists. In this particular case, Wire 1 breaks at the same time, and one crack is observed (see *Figure 4c* for detailed view). This crack initiation point has, on both sides, two darker areas marked with white circles (*Figure 4a*). These zones correspond to those under two contact pairs during the test, the angle between them support this idea (≈ 60º). The chemical compositions of these two dark zones and the contact mark between wires (*Figure 1a*) is analysed with the energy dispersive spectroscopy (EDS) technique. It is noted that the percentage in weight of oxygen is much higher (28%) at dark zones than that far from them (1%). This observation suggests that, when the crack is open, fretting debris produced at the contact pair, penetrate inside the crack producing these darker or rusted zones.

Figure 4d shows the same pattern as *Figure 4b*, two cracks initiate at Wire 5, where there is no contact with other wires.

It can be roughly concluded that wires break due to global stresses produced by the combination of bending moments and axial forces. In light of these preliminary results, it seems to be that fretting fatigue is not a determining factor in a 7-wire strand.

3. NUMERICAL MODEL.

Considering the strand size, stress and strain measurements are difficult because there are not gauges small enough to be placed on the wires. In addition, the only way to know contact stresses are analytical or numerical procedures. Costello´s theory was initially applied to obtain the stresses produced by the bending moment [14]. However, the results obtained for the bending stresses were overestimated due to the small sheave diameter. Therefore, to determine the strand behaviour as comprehensively as possible, a complete finite element model is developed with the objective of obtaining the extreme values of the load cycle, σmin and σmax.

This section analyses real test boundary conditions in order to apply them to the numerical model. In addition, the element types, geometry and mesh are discussed. Finally, the considered material properties are explained.

3.1 MESH & BOUNDARY CONDITIONS.

First, experimental boundary conditions are studied to reproduce, as well as possible, the strand behaviour in the FEM model. *Figure 5* schematises the real behaviour observed during tests and the strategy that is followed to model it. The information obtained from the tests are the maximum and minimum values of the axial load P_{max} and P_{min}, respectively, and the bending load Q that is imposed by the maximum displacement dmax. The parameter Q is considered to be the maximum value because the minimum is zero.
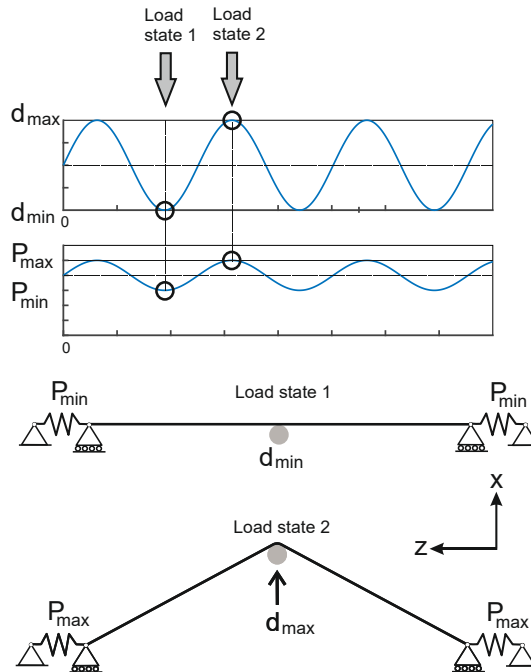
Figure. 5. Load analysis.

Therefore, the load cycle of the strand is defined by two load states. Load state 1 is the case in which the strand is subjected to the minimum displacement (d_{min} = 0). Therefore, the value of the axial load is P_{min}. Load state 2 is defined by the maximum bending displacement dmax, and thus, the axial load is P_{max}.

These boundary conditions are reproduced in the finite element model as shown in *Figure 6*. Only the effective length of the strand is modelled. Each end of the strand

has its displacement restricted in the x and y directions. A spring with a constant stiffness behaviour is placed at each side. The axial load of the spring P_s is P_{min} for load state 1 and P_{max} for load state 2. The remaining nodes of both springs are fully displacement-restricted. With these considerations, load state 1 is fully defined. The bending displacement of load state 2 (d_{max}) is applied by means of a rigid body with a 25 mm radius that is placed at the middle length of the specimen, resembling the sheave in actual tests.
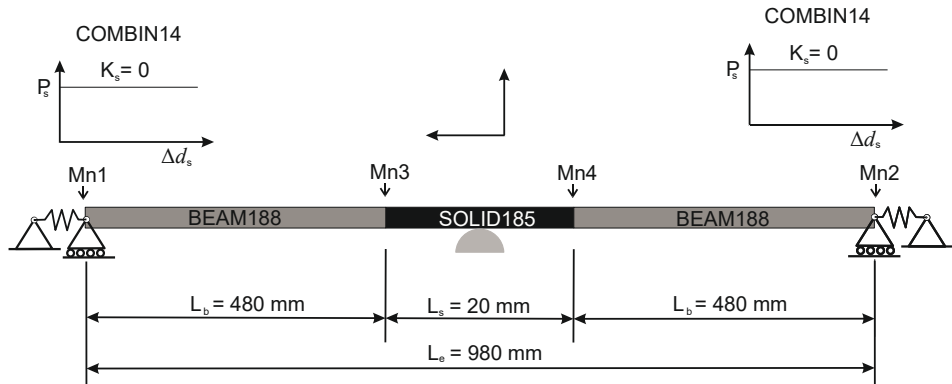

Figure 6. FEM model specifications.

The geometry of the strand in the FEM model is constructed with two different element types (see *Figure 6*) in ANSYS APDL 15 with implicit formulation. As shown in *Figure 6*, the effective length is divided into three parts. The central part, which is the most interesting part from the perspective of fatigue, is meshed with the SOLID185 element type with a first-order formulation, wherein the mesh is coarse far from the contact zones and is very fine near the contact zones (see *Figure 7*). The length of the solid mesh L_s is 20 mm and is discretized longitudinally with 124 elements. The mesh size in the vicinity of contact zones is approximately 4 μm. Therefore, the section of the smallest brick elements is 4 μm x 4μm. The influence of the number of longitudinal solid elements was studied comparing the results with 124 and 62 elements for the same L_s, concluding that the maximum stress variation was lower than 3%.

Figure 7 shows a section of the middle part of the FEM model with an example of the first principal stress obtained and the mesh refinement in the vicinity of the contact zone for Test 31 of Table 2. Wire 2 is not shown to show the mesh refinement and the stress values along one contact pair.

On each side of the solid part, the remaining strand length is modelled with BEAM188. Each element is defined by two nodes and a 1-dimensional element. The length of each beam part L_b is 480 mm, being the length of each beam element 0.33 mm.

The degrees of freedom of SOLID185 are displacements, whereas BEAM188 elements also include rotations. The coupling of solid and beam elements (Mn3 & Mn4 in *Figure 6*) is performed with master nodes and the CERIG APDL command. Each solid wire is coupled with its matching beam wire. Thus, 7 independent couplings are defined at each side of the solid block which join beam and solid degrees of freedoms. The springs are modelled by means of the COMBIN14 element, which is defined by the axial load Ps and zero stiffness $K_s = 0$. Springs are coupled with beam elements by means of master nodes 1 and 2 (Mn1 & Mn2 in *Figure 6*).

Contact elements between solid elements are defined with CONTA173 and TARGE170. Contacts between beams are defined with CONTA176 and also TARGE170, with parallel beam contact type, which is applicable for continuous contact type. The contact algorithm used is the augmented Lagrangian method and non-linear geometrical option is active. The total number of nodes is around 843000, which implies more than 2.5 million degrees of freedom.
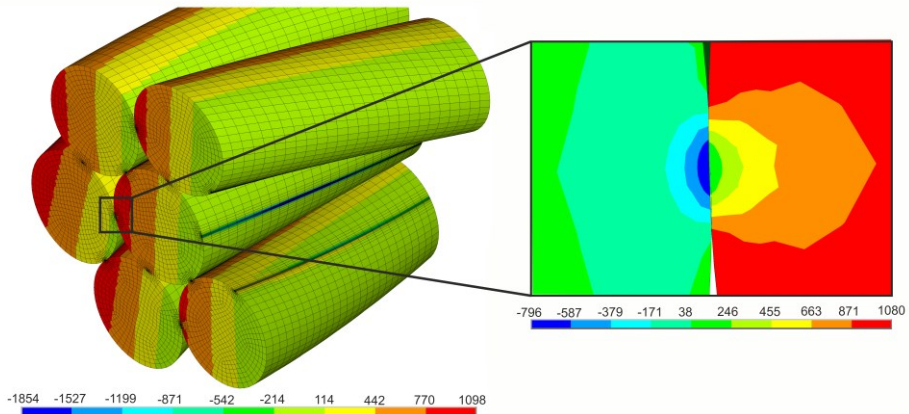

Figure 7. FEM model load state 2. First principal stress. σ₁ (MPa). Test 31.

Contact elements between solid elements are defined with CONTA173 and TARGE170. Contacts between beams are defined with CONTA176 and also TARGE170, with parallel beam contact type. The contact algorithm used is the augmented Lagrangian method. The non-linear geometry option is active due to the large displacements produced by the bending load.

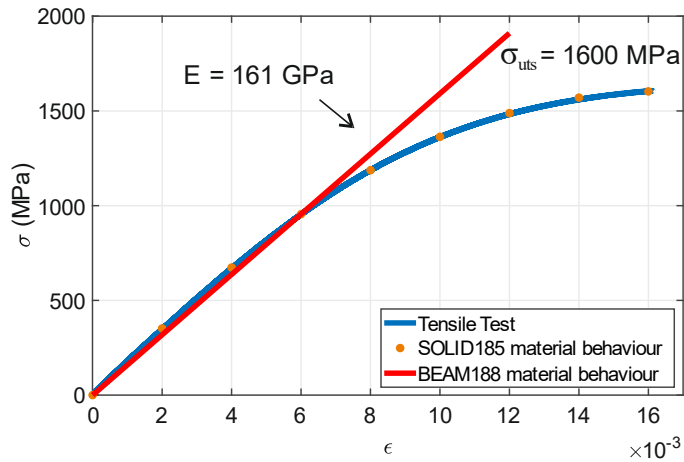**3.2. MATERIAL PROPERTIES.**

Figure 8. Material tensile test and FEM material model considered.

To obtain the mechanical properties of the material, some static traction tests were performed with the inner wire of the strand. *Figure. 8* shows the actual stress-strain curve obtained for the inner wire. The choice of the inner wire for this purpose is based on the wire geometry, as only the inner wire is straight. In *Figure 8*, the points indicate the discretization implemented for the material behaviour for solid elements in the numerical model. Beam elements do not support material non-linearity; therefore, an elastic behaviour is assumed. In any case, this is correct because this part of the strand is only subjected to an axial load and the stresses are below 430 MPa. The Young's modulus considered for the elastic behaviour is 161 GPa, a value that agrees well with stresses under 1000 MPa. The Poisson coefficient is considered as $v = 0.3$.

The friction coefficient μ is the second material parameter required for the model. The friction coefficient between two steel surfaces subjected to variable loading

after more than 1000 cycles is considered to be between 0.6 and 0.9 [25-26]. A value of 0.8 is used in the model. In view of the type of failure observed, which mainly occurs far from contact zones, this parameter is not vital because it has major effect on the stresses close to contact zones and minor far from them.

4. RESULTS

Before applying the finite element model, a pair of validations were carried out. The first validation is performed for load state 1 and shown in *Figure 9a*, which shows the axial stress produced at Wire 1 because of an axial load P, considering a linear elastic behaviour and frictionless contact. Thus, the results can be compared with the analytical expression obtained from [27] and simplified for a 7-wire strand (*Equation (1)*).

$$\sigma = \left(A_1 + \frac{\cos^3(\alpha)}{1 + v\sin^2(\alpha)} A_{27} \right)^{-1} P \tag{1}$$

Where A_1 is the area of Wire 1, A_{27} the sum of the outer layer wire areas.

In addition, a second validation is performed for load state 2. During tests, P_m and d_{max} are imposed, and thus, P_{max} and Q_{max} are obtained via load cells. Imposing $P_s = P_{max}$ and d_{max} to the numerical model, the maximum force that produces bending, Q, can be obtained. *Figure 9* shows the agreement between test and numerical results for a specific value of d_{max} and different P_{max} loads. Note that for low axial load values, the scattering and error are higher than those associated with high loads, which attributes to the inherent control system of the actuators that it could not move exactly in phase both cylinders for low axial loads. However, the scattering and error decrease as the axial load increases. Therefore, the finite element model is considered to be acceptable because the error and scattering are associated with real test values.

In view of the experimental results, it is expected that maximum stresses will be found at points of maximum bending moment. It is clear that failure is governed by axial stress σ, which also coincides with principal maximum stresses far from contact surfaces. Henceforth, references to stress values refer to the axial direction.
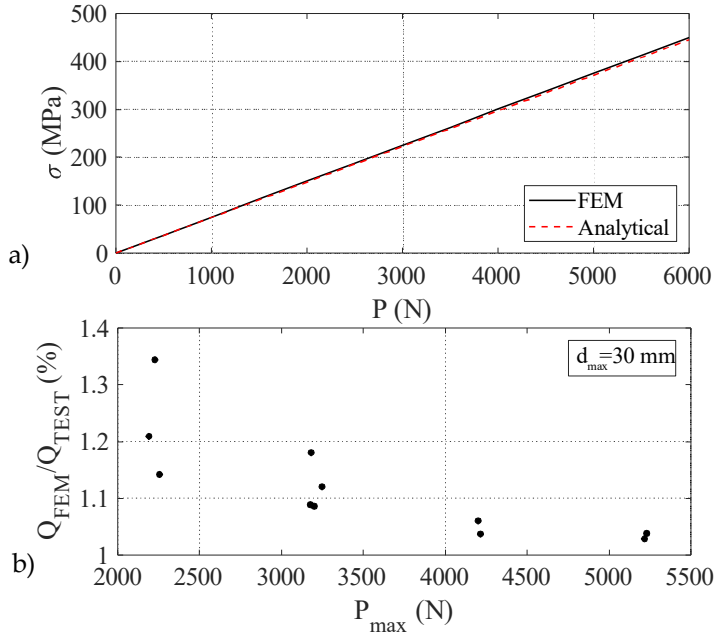
Figure 9. a) Comparison between numerical and analytical results, b) FEM and tests load correlation.

Therefore, axial stress σ of load state 2 is studied for cases along different paths at the middle length of the strand, as shown in *Figure 10*. Along paths 1 and 2, σ is obtained for the strand FEM model. Path 2 forms 10 degrees to the horizontal to study the stresses produced far enough from the contact pair to avoid its influence. Path 1 crosses the contact zone, and it is observed that contact produces a compression field that prompts a decrease in the axial stress value. However, maximum axial stresses with a non-negligible gradient are noticed in Wire 5, which agrees with the type of failure observed. Maximum stresses and gradients of path 2 (Wire 1) are quite similar to those observed in Wire 5. This analysis is a way to explain why in some cases Wires 1 and 5 break at the same time: both are subjected to similar axial stresses and gradients. In cases in which Wire 1 fails, the initiation is observed between contact zones, which are far from the compression field produced by contact stresses (see *Figure 4a*).
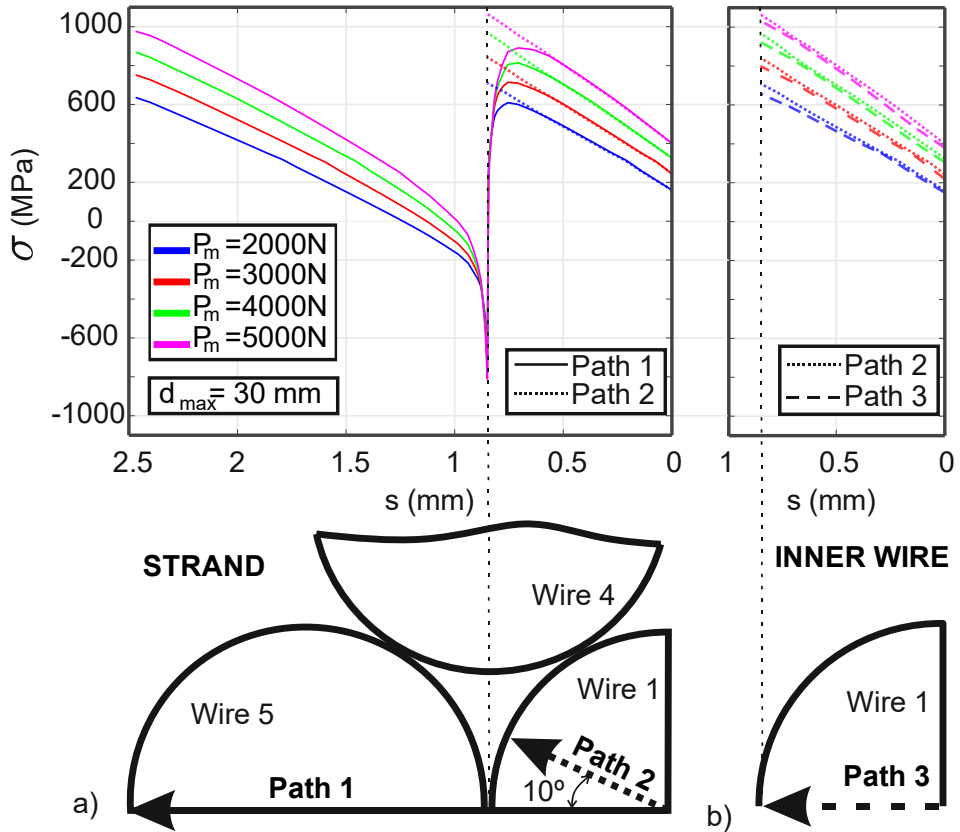
Figure 10. Axial stress along different paths for load state 2. a) Comparison of FEM strand paths 1 and 2, b) Comparison of FEM wire path 3 and FEM strand path 2.

In view of these results, it is possible to analyse the strand as independent wires because the failure is produced far from the interaction between bodies and coincides with the maximum axial stress. Therefore, a simplified FEM model is analysed. This simplified model considers only Wire 1 using the same effective length, material behaviour and boundary conditions used for the strand FEM model. However, two small modifications must be made to compare the results. The punch radius in this case is augmented by the diameter of an outer wire. As such, the new punch radius is 26.2 mm, which reproduces the same curvature as in the strand FEM model, which is facilitated by applying the same value of d_{max}. The second modification is the spring load. According to the geometry approximately a

15% of the total axial load is assumed by the inner wire for the parameters used such that the value of the springs in the simplified model is P_{sw} = 0.15 P_{max}. The results are shown in *Figure 10b* (Path 3). The axial stress values and gradients observed along path 3 are similar to those in path 2, which were also similar to those in path 1 for Wire 5. Therefore, the axial stress of load state 2 (σ_{max}) for this specific strand configuration and boundary conditions could be obtained with the simplified FEM model, analysing only Wire 1. Thus, the axial stress of load state 2 is obtained from the simplified FEM model, in which dmax and P_{sw} = 0.15 P_{max} are imposed; the results are shown in *Table 2*.

The stress of load sate 1, σmin, is obtained in the same way. That is, by means of the simplified FEM model, but in this case imposing only the axial load to the spring as *Psw* = 0.15 *Pmin*. Henceforth, references to FEM results are referred to as the simplified model.

To consider the elastic-plastic behaviour of the material, at least one pair of cycles must be taken into account to estimate an accurate value of σ_{min}. A significant strain hardening effect occurs for values higher than 1000 MPa. For lower values, the behaviour could be considered linear elastic with negligible error, as shown in *Figure 8*. The unloading process was simulated in the FEM model, for which strong convergence problems arose. Therefore, in order to calculate an accurate value of σmin at the outer surface of Wire 1 while considering plasticity, the following procedure is performed with the simplified FEM model.

At first, the stress of load state 2 is calculated with the elastic-plastic simplified model. Then, to estimate the stress at load state 1, the unloading process is considered to be purely elastic. Therefore, a linear elastic simplified FEM model is performed with Wire 1, with the aim of estimating the maximum axial stress at load state 2 σ_{max}^e (see *Table 2*). *Figure 11* schematises the procedure to obtain the value of σmin. The minimum elastic axial stress σ_{min}^e is obtained by analytically applying *Equation (2)*.
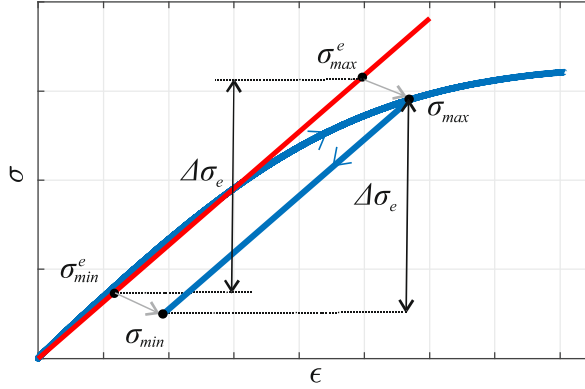
$$\sigma_{min}^e = \frac{0.15 P_{min}}{A_1} \tag{2}$$

Figure 11. Procedure developed for obtaining σ$_{min}$ in function of σ$_{max}$ and Δσ$_e$

Therefore, with these values, an elastic stress range *Δσ$_e$* is obtained according to *Equation (2)*. Assuming that the unloading process is performed with an elastic behaviour, the same range is applicable to the elastic-plastic unloading process, as shown in *Figure 11*. Therefore, the value of *σ$_{min}$* that accounts for the strain hardening effect could be estimated by applying *Equation (3)*.

$$\Delta\sigma_e = \sigma_{max}^e - \sigma_{min}^e \tag{3}$$

$$\sigma_{min} = \sigma_{max} - \Delta\sigma_e \tag{4}$$

Table 2 shows the loading parameters and FEM results obtained in all tests. The value Pmt is the theoretical mean axial load value, which in conjunction with dmax, defines each test. As shown, for the same combinations of Pmt and dmax, slightly different *P$_{max}$*, *P$_{min}$* and *Q* values are obtained. Instead of reproducing FEM simulations for each test, average values of *P$_{max}$* and *P$_{min}$* are used. Therefore, 19 load combinations were accounted for in the FEM simulation process.

Table 2. Test and FEM results.

| Test	P_{mt} (N)	d_{max} (mm)	P_{max} (N)	P_{min} (N)	Q (N)	Cycles	σ_{max} (MPa)	σ^e_{max} (MPa)
1	2000	30	2191	1822	289.0	128350		
2	2000	30	2225	1782	259.9	175100	669	715
3	2000	30	2254	1745	306.1	188727		
4	2000	40	2301	1700	391.0	84850	852	928
5	2000	50	2459	1548	481.1	119300		
6	2000	50	2478	1560	523.1	80200	1037	1164
7	2000	50	2449	1549	526.4	67750		
8	3000	20	3122	2921	391.0	763100	608	645
9	3000	20	3104	2898	231.3	$>10^6$		
10	3000	30	3180	2823	401.0	72700		
11	3000	30	3176	2806	435.8	71450	813	881
12	3000	30	3247	2777	422.5	79050		
13	3000	40	3305	2712	585.6	47350		
14	3000	40	3306	2682	590.8	63400	1011	1123
15	3000	40	3309	2706	573.7	61859		
16	3000	50	3454	2540	717.7	33855		
17	3000	50	3454	2533	729.6	21515	1191	1383
18	3000	50	3453	2593	715.8	28378		
19	4000	20	4106	3881	385.8	133763	719	767
20	4000	20	4128	3881	375.3	193000		
21	4000	30	4214	3805	584.1	81050	942	1027
22	4000	30	4199	3819	571.3	59017		
23	4000	40	4328	3690	752.0	33055		
24	4000	40	4328	3685	746.7	33321	1137	1302
25	4000	40	4356	3642	742.5	27385		
26	4000	50	4480	3524	921.0	18525		
27	4000	50	4476	3556	921.8	15182	1311	1584
28	4000	50	4476	3504	904.1	18431		
29	5000	20	5153	4911	487.3	535400	806	806
30	5000	20	5135	4881	451.6	147050		
31	5000	30	5217	4792	722.0	87050	1044	1165
32	5000	30	5230	4804	715.3	40400		
33	5000	40	5348	4651	934.2	32534		
34	5000	40	5649	4695	935.6	20450	1251	12477
35	5000	40	5385	4660	926.0	19210		
36	5000	50	5515	4486	1165.0	16445	1405	1757
37	5000	50	5518	4518	1094.0	11764		
38	6000	20	6156	5885	538.8	225800	907	946
39	6000	30	6235	5774	801.1	53950	1137	1295
40	6000	30	6253	5770	791.1	41948		
41	6000	40	6392	5631	1058.0	19880	1336	1611
42	6000	50	6572	5475	1307.0	9980	1484	1915

5. LIFE PREDICTION.
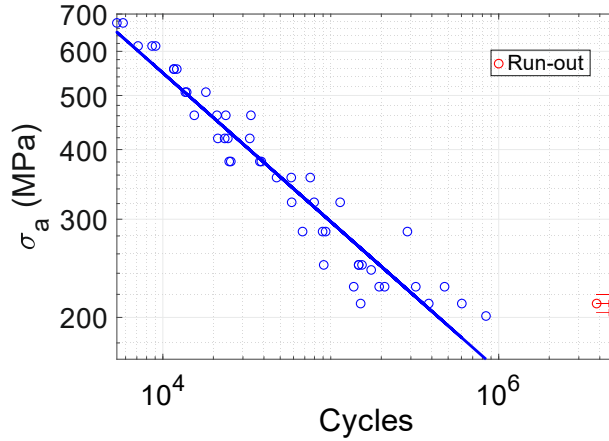
Figure 12. Material S-N curve data and fit. R=0.1.

Once the stresses of the experimental tests are known, the next step is establishing the relation between the damage parameter and the life obtained. An S-N curve of the material in axial loading is obtained after testing 50 inner wires of the strand with $R = 0.1$ (*Figure 12*). A fatigue limit near 212 MPa is obtained supported by three run-out tests.

The stress ratio R for the tests performed with the strand under axial and bending loads is different for each test. From *Table 1* and applying *Equations (4)* and *(5)*, mean stress (σ_m) and stress amplitude (σ_a) can be obtained.

$$\sigma_a = \frac{\sigma_{max} - \sigma_{min}}{2} \tag{5}$$

$$\sigma_m = \frac{\sigma_{max} + \sigma_{min}}{2} \tag{6}$$

Therefore, to compare strand test results with the S-N curve of the material and include the effect of mean stress, the Walker equation is applied [28]. This expression is shown by *Equation (7)*, where the parameter γ must be estimated by means of the procedure shown in the aforementioned reference [28]. The value obtained is 0.6 adjusted according to the obtained numerical results, which is

similar to the value given by reference [28] for this material as a function of σ_{uts}.

$$\sigma_w = \sigma_{max} \left(\frac{1-R}{2}\right)^\gamma \tag{7}$$

The value σw is considered to be the stress amplitude with the load ratio $R = -1$ (zero mean stress), for which the same life level as the actual combination of σa and σm is obtained. Therefore, applying *Equation (6)* to both strand and wire S-N curve data, it is possible to compare them with the same load ratio. The stress amplitude of the wire S-N curve σa can be obtained directly from *Figure 12*, and mean stress value σm can be easily obtained if the load ratio ($R = 0.1$) is known.

In addition to the effect of mean stress, there is a remarkable difference between the S-N curve of the material and the fatigue strand test. The wire fatigue tests were performed with axial loading, and therefore, there was not a stress gradient. However, the bending moment applied to the strand produces severe gradients, as was shown earlier (*Figure 10*). The existence of a stress gradient is the reason for the higher fatigue strength in bending fatigue than in axial fatigue, given the same maximum stress. It is widely recognized in the fatigue field and used in real practice that the fatigue strength in axial loading is between 0.7 and 0.9 times the one in bending [29–30]. Any fatigue model has to take this effect into account. That is why, in order to compare the fatigue curve of the strand with the curve of the wire, the former will be divided by a factor of 0.8. This value is in the middle of the range given before.

Figure 13 shows the adjusted line for the material S-N curve and the adjusted line of the strand test after applying *Equation (7)*. In addition to these lines, the stress values for each strand test are shown, grouped as a function of dmax. As shown, in general, the higher the displacement, the lower the life.
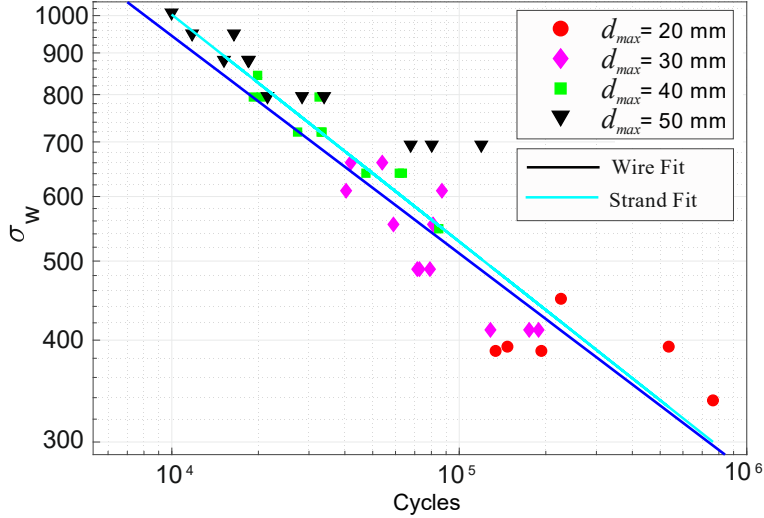
Figure 13. Material and strand adjustment with the Walker relation.

Figure 13 shows the adjusted line for the material S-N curve and the adjusted line of the strand test. In addition to these lines, the stress values for each strand test that are obtained after the application of the Walker equation are shown, grouped as a function of d_{max}. As shown, in general, the higher the displacement, the lower the life.

Very good agreement is observed between the wire S-N curve and the strand S-N curve. This means that the fatigue life in any strand test could be estimated based on the stresses calculated with FEM and the fatigue curve of the material. Both are modified by means of the Walker equation, which also depends on the value of γ, which is adjusted with the tests presented herein. The same procedure was carried out with other models that take into account a non-zero mean stress, such as Goodman [31], Gerber [32] or Smith-Watson-Topper [33], as shown by *Equations (7)* to *(9)*, where $\Delta\varepsilon$ is obtained as $\Delta\sigma_e/E$.

$$\sigma_{Goodman} = \frac{\sigma_a}{1 - \frac{\sigma_m}{\sigma_{uts}}} \tag{8}$$

$$\sigma_{Gerber} = \frac{\sigma_a}{1 - \left(\frac{\sigma_m}{\sigma_{uts}}\right)^2} \tag{9}$$

$$\sigma_{SWT} = \sqrt{\sigma_{max} E \Delta\varepsilon}$$

(10)

Finally, the results are shown in *Figure 14*. Note that good agreement is observed independently of the stress modifications used, although the Walker modification agrees better with the material curve followed by the SWT parameter. The advantage of the SWT parameter is that no additional parameters are required for model correction compared with the Walker model.
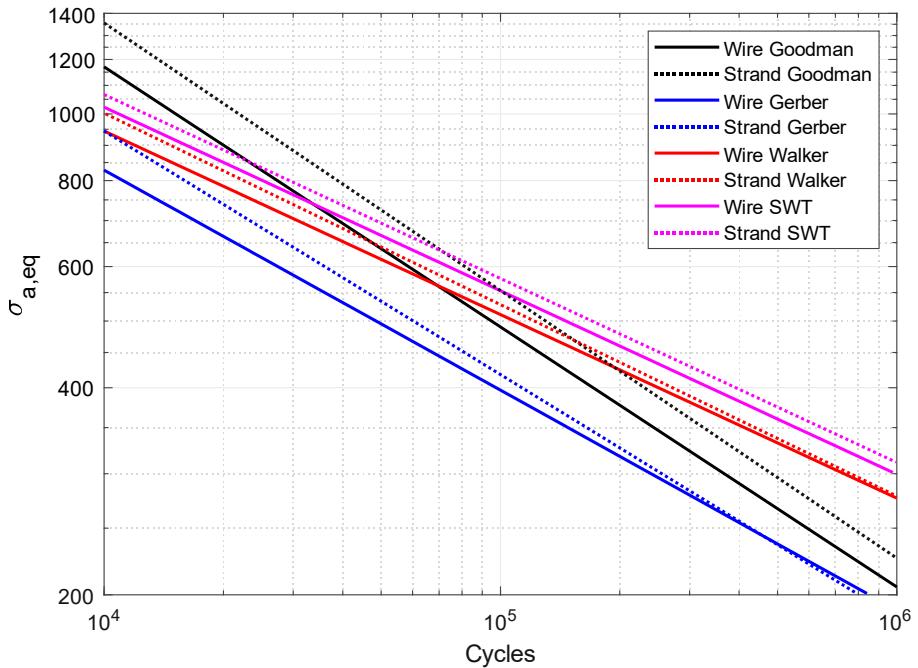

Figure 14. Comparison of S-N curves.

6. CONCLUSIONS.

The fatigue failure of a 7-wire stainless steel strand is studied. Several tests are performed by applying different combinations of axial and bending loads. Fracture surfaces are analysed using a scanning electron microscope, and the results suggest

that the failure of the strand is due to global stresses rather than fretting. To determine the stress and strain fields of the specimen, a complete finite element model is built to reproduce the experimental tests as faithfully as possible including friction and nonlinear material behaviour. The results of the FEM model are consistent with the type of failure observed and are used to estimate the strand S-N curve.

The material S-N curve is compared with the strand one applying different methods to obtain an equivalent stress. Very good fitting is observed between material and strand S-N curves, independently of the methodology used to consider mean stress.

We conclude that if the failure of a 7-wire strand is avoided close to the clamps, then failure seems to be produced by global stresses. It is also observed that the boundary conditions of the strands are vital for the fatigue life, specifically those related to the clamp system.

ACKNOWLEDGEMENTS

REFERENCES

[1] Zhou ZR, Cardou A, Fiset M, Goudreau S. Fretting fatigue in electrical transmission lines. *Wear*. 1994; 173(1-2):179–188.

[2] NJ Gimsing, Georgakis CT. *Cable Stayed Bridges: Concept and Design*. United Kingdom: Wiley Press; 2011.

[3] Peterka P, Krešák J, Kropuch S, Fedorko G, Molnar V, Vojtko M. Failure analysis of hoisting steel wire rope. *Eng Fail Anal*. 2014; 45: 96–105.

[4] Pal U, Mukhopadhyay G, Sharma A, Bhattacharya S. Failure analysis of wire rope of ladle crane in steel making shop. *Int. J. Fatigue*.2018;116:149–155.

[5] Fadel AA, Rosa D, Murça LB, Fereira JLA, Araújo JA. Effect of high mean tensile stress on the fretting fatigue life of an Ibis steel reinforced aluminium conductor. *Int J Fatigue*.2012;42:24–34.

[6] Hobbs RE, Raoof M. Mechanism of fretting fatigue in steel cables. *Int J Fatigue*. 1994;16(4)273–280.

[7] Zhou ZR, Cardou A, Goudreau S, Fiset M. Fundamental investigations of electrical conductor fretting fatigue. *Tribol Int.* 1996;29(3)221–232.

[8] Winkler J, Georgakis CT, Fischer G. Fretting fatigue behavior of high-strength steel monostrands under bending load. *Int J Fatigue*.2015;70:13–23.

[9] Chen Y, Meng F, Gong X. Interwire wear and its influence on contact behavior of wire rope strand subjected to cyclic bending load. *Wear.* 2016;368:470–484.

[10] Mohammed Raoof REH. Analysis of multilayered structural strands. *J Eng Mech*.1988;114:1160–1182.

[11] Raoof M. Axial fatigue of multilayered strands. *J Eng Mech*.1990;116(10)2083–2099.

[12] Raoof M. Free-bending fatigue life estimation of cables at points of fixity. *J Eng Mech*.1992;118(9):1747–1764.

[13] Azevedo CRF, Henriques AMD, Pulino Filho AR, Ferreira JLA, Araújo JA. Fretting fatigue in overhead conductors: rig design and failure analysis of a Grosbeak aluminium cable steel reinforced conductor. *Eng Fail Anal*. 2009;16(1): 136–151.

[14] Costello GA. *Theory of Wire Rope*. New York: Springer Science & Business Media; 1997.

[15] Cardou A, Jolicoeur C. Mechanical Models of Helical Strands. *Appl Mech Rev*.1997;50(1)1–14.

[16] Usabiaga H, Pagalday JM. Analytical procedure for modelling recursively and wire by wire stranded ropes subjected to traction and torsion loads. *Int J Solids Struct.* 2008;45(21)5503–5520.

[17] Wokem C, Joseph T, Curley M. Fatigue life prediction for cables in cyclic tension. *J Strain Anal Eng Des*.2018;53(5):141–155.

[18] Song B, Wang H, Cui W, Liu H, Yang T. Distributions of stress and deformation in a braided wire rope subjected to torsional loading. *J Strain Anal Eng Des*.2019;54(1):3–12.

[19] Beltrán JF, Nuñez E, Nuñez F, Silva I, Bravo T, Moffat R. Static response of asymmetrically damaged metallic strands: Experimental and numerical approach. *Constr Build Mater*.2018;192:538–554.

[20] Kim JK, Yang JM. Effect of design variables on deflected tensile performance of high-strength 7-wire steel strand for stay cable. *Constr Build Mater*. 2018;188:40–48.

[21] Lalonde S, Guilbault R, Langlois S. Modeling multilayered wire strands, a strategy based on 3D finite element beam-to-beam contacts - Part II: Application to wind-induced vibration and fatigue analysis of overhead conductors. *Int J Mech Sci*., vol. 126, pp. 297–307, 2017.

[22] Jiang WG, Yao MS, Walton JM. A concise finite element model for simple straight wire rope strand. *Int J Mech Sci*. 1999;41(2):143–161.

[23] Jiang WG, Yao MS, Walton JM. Concise finite element model for three-layered straight wire rope strand. *Int J Mech Sci*. 2000;42(1):63–86.

[24] Erena D, Vázquez J, Navarro C, Domínguez J. New fatigue device for testing cables: Design and results. *Fatigue Fract Eng Mater Struct*. 2019;42:1826-1837.

[25] Juoksukangas J, Lehtovaara A, Mäntylä A. A comparison of relative displacement fields between numerical predictions and experimental results in fretting contact. *Proc Inst Mech Eng Part J J Eng Tribol*.2016;230(10):1273–1287.

[26] Hintikka J, Lehtovaara A, Mäntylä A. Fretting-induced friction and wear in large flat-on-flat contact with quenched and tempered steel. *Tribol Int*.2015;92:191–202, 2015.

[27] K. Feyrer, *Wire ropes: Tension, endurance, reliability*. 2015.

[28] Dowling NE, Calhoun CA, Arcari A. Mean stress effects in stress-life fatigue and the Walker equation. *Fatigue Fract Eng Mater Struct*.2009;32(3):163–179.

[29] Budynas RG, Nisbett JK. *Shigley's Mechanical Engineering Design, 8th ed*. New York: McGraw-Hill; 2008.

[30] Lee YL, Pan J, Hathaway R, Barkey M. *Fatigue testing and analysis: Theory and practice*. Oxford: Butterwoth-Heinemann; 2005.

[31] Goodman J, Mechanics applied to engineering. London: Longmans, Green; 1919.

[32] Gerber WZ. Bestimmung der Zulossigen Spannungen in Eisen Constructionen. *Z Bayer Archit Inger Ver*.1874;6:101.

[33] Smith KN, Watson P, Topper TH. A stress-strain function for the fatigue of metals. *J Mater*.1970;5(4):767–778.